Phase transitions, domain structure and pseudosymmetry in La- and Ti-doped $BiFeO_3$

Amir Khesro[1], Rebecca Boston[1], Iasmi Sterianou[2], Derek C. Sinclair[1] and Ian M. Reaney[1].

1. Functional Materials and Devices, Materials Science and Engineering, Sir Robert Hadfield Building, University of Sheffield, Sheffield, S1 3JD, UK.
2. Materials and Engineering Research Institute, Sheffield Hallam University, Howard Street, Sheffield, S1 1WB, UK.

Abstract

The phase transitions and domain structure of the promising PbO-free solid solution series, *(0.95-x)*$BiFeO_3$ - *x*$LaFeO_3$ - *0.05*$La_{2/3}TiO_3$ were investigated. X ray diffraction (XRD) revealed a transition from a ferroelectric (FE) *R3c* to a $PbZrO_3$ (PZ) -like (*Pbam*) antiferroelectric (*AFE*) structure at $x = 0.15$ followed by a transition to a paraelectric (PE, *Pnma*) phase at $x > 0.30$. The ferroelastic/ferroelectric twin domain width decreased to 10-20 nm with increasing *x* as the AFE phase boundary was approached but coherent antiphase tilted domains were an order of magnitude greater. This domain structure suggested the local symmetry (20 nm) is lower than the average structure (*R3c*, $a^-a^-a^-$) of the tilted regions. The PE phase ($x = 0.35$) exhibited a dominant $a^-a^-c^+$ tilt system with *Pnma* symmetry but diffuse reflections at ~1/4{*ooe*} positions suggest that short range antipolar order is residual in the PE phase. The complex domain structure and phase assemblage of this system challenge the conventional interpretation of phase transitions based on macroscopic symmetry. Instead, it supports the notion that frustration driven by chemical distributions at the nanometric level influence the local or pseudo-symmetry as well as the domain structure, with XRD giving only the average macroscopic structure.

Introduction

$BiFeO_3$ (BFO) is one of the most extensively researched perovskite compounds because of its room temperature multiferroic properties. It is simultaneously ferroelectric (FE) with a Curie temperature, $T_C \approx 1100$ K,[1] and antiferromagnetic (AFM) with a Néel temperature $T_N \approx 643$ K.[2] The magnetic ordering is G-type with a weak canting moment with a 62 nm spin cycloid.[3] At room temperature, the unit cell of BFO is rhombohedral (*R3c*) with a_{rh} of 5.6343 Å, α_{rh} of 59.348° and a ferroelectric axis along $[111]_p$ (*p* = pseudocubic).[4,5] The polarization of BFO is reported to be very large (ca. 90-100 μC/cm^2) and hence it has attracted considerable attention for potential use in next generation ferroelectric memories.[6-8] Generally, polarization versus electric field loops do not saturate due to a combination of high Curie temperature (T_C) and conductivity.[9] As a room temperature multiferroic, BFO is an obvious choice for applications such as multiple state memory elements, electric field controlled magnetic resonance devices and transducers with magnetically modulated piezoelectricity.[10] One of the issues currently facing BFO is that the multiferroic properties are inaccessible due to its antiferromagnetic nature, which leads to cancellation of macroscopic magnetization and generally hinders linear magnetoelectric coupling.[11] Moreover, the processing of phase-pure BFO is very difficult and is usually associated with parasitic phases such as $Bi_{25}FeO_{39}$ and $Bi_2Fe_4O_9$, due also in part to the volatile nature of Bi_2O_3.[12]

Partial substitution of rare earth (RE) ions on the A-site of BFO have been shown to reduce T_C, eliminate secondary phases and enhance the magnetic properties.[1] An antiferroelectric (AFE) $PbZrO_3$-like structure is also reported to be stabilized between the FE, *R3c* and PE, *Pnma* phases in RE-doped BFO.[9,13] It has also been postulated that during processing Fe^{3+} reduces to Fe^{2+}, compensated by the formation $V_O^{\cdot\cdot}$, leading to an increase in conductivity.[14] Hence, researchers have adopted a strategy of donor doping on the B-site to reduce the $[V_O^{\cdot\cdot}]$, thereby enhancing resistivity.

Doping Ti^{4+} ions in $Bi_{0.85}Nd_{0.15}FeO_3$ has shown promising results by reducing bulk conductivity from ~1 mS cm^{-1} to <1 μS cm^{-1}, accompanied by a large increase in activation energy for bulk conduction from 0.29 to >1.0 eV.[15] Recently Reaney *et al.*[16] investigated $Bi_{0.85}Nd_{0.15}Fe_{0.9}Ti_{0.1}O_3$ using aberration corrected scanning transmission electron microscopy and found a distribution of Nd-rich precipitates in the perovskite matrix, concluding that Ti donor-doping is ionically compensated by V_{Nd}''' rather than V_{Bi}''' or V_{Fe}'''. The authors proposed the appropriate tie-line for preparing single-phase compositions should be based on the solid solution, $RE_{2/3}TiO_3$ - $BiFeO_3$. Our initial studies on the system $xRE_{2/3}TiO_3$ - $(1-x)BiFeO_3$ revealed only a limited solubility of x ~ 0.03 and ~0.05 for RE = Nd and La, respectively. Hence, to extend the RE-doping concentration levels, $LaFeO_3$ is used as an alternative end member within a ternary $(0.95-x)BiFeO_3$ - $xLaFeO_3$ - $0.05La_{2/3}TiO_3$ (BLFT) solid solution series. The resulting ceramics revealed themselves to have a homogeneous distribution of the constituent ions compared with $(1-x)BiFeO_3 - xLaFeO_3$ compositions, possibly as a result of the enhanced diffuse rates due the formation of A-site vacancies. Consequently not only could the functional properties be investigated but also phase transitions occurred over narrow compositional and temperature intervals in comparison to previous studies.[9] Hence, these compositions afforded a more detailed study of the domain and local structure using transmission electron microscopy.

Methodology

BLFT ($0.05 \leq x \leq 0.35$) solid solutions as shown in Figure 1 were prepared using Bi_2O_3 (99.9 %, Acros Organics), Fe_2O_3 (99%, Sigma Aldrich), TiO_2 (99.9 %, Sigma Aldrich) and La_2O_3 (99.99 % Stanford Materials) as the starting materials. The raw materials were dried before use.

Samples were attrition milled for 1 hour at 300 rpm in a Union Processes Attritor (Szegvari Attritor System, Union Process, Arkon, Ohio, USA) attrition mill, using 3 mm diameter yttria-stabilised zirconia media in isopropanol. The slurry was separated from the media and dried overnight at 80 ˚C. The mixed dried powders were then sieved through a 355 micron mesh and calcined at temperatures between 910-990 °C for ($0.05 \leq x \leq 0.35$) in Al_2O_3 crucibles for 3 hours at 3 ˚C/min in a muffle furnace.

The calcined powders were attrition milled for a second time as above, and then pressed into pellets using a uniaxial press. The green pellets were sintered in air at various temperatures in the range 960-1060 °C for ($0.05 \leq x \leq 0.35$) for 3 h at 3 ˚C/min to achieve > 95% of the theoretical density. Bulk densities were measured using a Mettler Toledo model MS104S digital densitometer utilising the Archimedes principle.

XRD was performed on crushed pellets using a Siemens D5000 diffractometer with CuKα (λ = 1.5418 Å). *In situ* XRD was performed for selected samples using a Siemens D5000 HTXRD and data were collected in the temperature range 30 – 500 °C. Differential

scanning calorimetry (DSC) was performed using a Netzch DSC 404 C Pegasus from 20 to 800 °C at heating/cooling rates of 10˚/min.

For scanning electron microscopy (SEM) the samples were mounted on aluminium stubs and coated with carbon. SEM of fracture surfaces was performed using a JEOL JSM-6400. Samples for Transmission Electron Microscopy (TEM) were mechanically ground to a thickness of ~50 µm, mounted on copper rings and ion-milled until perforated using a Gatan Duo Mill. Electron diffraction patterns and images were taken using a JEF-2010F TEM, operating at 200 kV.

For dielectric measurements, gold paste electrodes (T-10112, Metalor Technologies UK Ltd., Birmingham, UK) were applied to the pellets, which were then heated at 800 °C for 2 h to harden and anneal. A LCR meter (Model 4284A, Hewlett Packard, HP) was used to measure capacitance and tan δ at fixed frequencies of 100 kHz, 250 kHz and 1 MHz from room temperature to 800 °C. A HP4192A was used to perform impedance spectroscopy (IS) at various temperatures between 25 and 500 °C in the frequency range 5 Hz to 13 MHz.

A RT66A standardized ferroelectric test system (Radiant Technologies) operated in virtual ground mode coupled to a TREK high voltage amplifier (Model 609E-6) was used to generate room temperature polarisation-field (P-E) data for the fabricated ceramics. To achieve high saturation field the samples were mechanically thinned to less than 0.5 mm before electroding. The data were recorded by placing the sample in Silicone oil between Cu electrodes.

Results and Discussion

XRD traces from crushed pellets of BLFT ($0.05 \leq x \leq 0.35$) are shown in Figure 2. All compositions could be indexed according to single phase perovskite structure with no secondary peaks observed within the detection limit of the diffractometer. The peaks in compositions with $x \leq 0.10$ were indexed as a FE phase with rhombohedral (*R3c*) symmetry. Peak splitting was observed at $x = 0.15$ which persisted until $x \leq 0.30$. This was attributed to the transformation from the ferroelectric phase to the antiferroelectric $PbZrO_3$-like (*Pbam*) structure reported by *Karimi et al.* for Nd-doped $BiFeO_3$.[13] At $x = 0.35$, the splitting disappeared resulting in metrically cubic XRD patterns. SEM images of fractured surfaces for $x = 0.05$ and $x = 0.15$ are shown in Figure 3. The microstructure is similar for all compositions with a grain size < 1 µm.

DSC data for a range of BLFT samples are shown in Figure 4 which reveal anomalies at ~ 715, ~ 651 and ~ 561 °C, for $x = 0.05$, 0.10 and 0.15, respectively. As the La concentration increases, the anomalies become broader and less intense and no discrete peaks were observed for compositions with $0.20 \leq x \leq 0.35$. The decrease in T_C with increasing x may be explained by considering that the onset temperature of the PE-FE and PE-AFE transitions decreases with decreasing tolerance factor (t) and average A-site ionic polarizability, α.[17] The tolerance factor establishes, in a single metric, how well the ions within the perovskite lattice fit in their respective sites.[18]

La^{3+} (1.32 Å, 5.5 $Å^3$) has smaller ionic radius and polarizability than Bi^{3+} (1.36 Å, 6.12 $Å^3$)[19], hence increasing La ion concentration decreases both t and α simultaneously. This has the effect of decreasing T_C with respect to the end member BFO and also promoting an AFE rather than FE phase.[9] A composition-independent anomaly at ~350 °C is observed in all DSC plots, indicating a transition from AFM ordering to a paramagnetic phase (T_N).

Magnetic ordering is dominated by the B-site, and hence substituting magnetic Fe^{3+} by diamagnetic Ti^{4+} ions results in a lower value of T_N compared to pure BFO.[15]

The relative permittivity and tan δ of samples with $0.05 \leq x \leq 0.35$ are shown in Figure 5. A broad relaxation is observed near T_N for all compositions. In BFO-based ceramics, such anomalies have been previously reported[11,20-23] but their underlying cause is not yet fully understood. Cheng *et al.*[21] attributed it to ferroelastic strain coupled with an antiferromagnetic transition. Others[22,23] have attributed it to Maxwell-Wagner-type relaxation which may arise due to space-charge polarization. The dielectric loss at room temperature is < 0.05 for all compositions but above ~ 300 °C it rises sharply. This is attributed to an increase in conductivity, which may also account for the anomalies near T_N. Above 500 °C, all compositions become highly conductive, and hence the transitions observed for ($0.05 \leq x \leq 0.15$) in DSC could not be observed in ε_r versus temperature plots. However, composition dependent, frequency independent broad peaks are observed in ε_r versus temperature for $x > 0.15$, which suggests they relate directly to the onset of the PE-AFE transition but further evidence is required to prove that the dielectric maxima are coincident with a change in symmetry.

In-situ XRD data for compositions $0.20 \leq x \leq 0.30$ are shown in Figure 6 (a-c). For $x = 0.20$, the peak splitting at ~ 45° 2θ starts to disappear at 300 °C and becomes undetectable by 400 °C. For $x = 0.25$, the peak splitting disappears at a lower temperature, between 250 and 300 °C, and similarly in $x = 0.30$ the peak splitting (albeit weaker) vanishes between 25 and 200 °C. *In-situ* XRD data thus confirms that the broad dielectric maxima correspond to a change in symmetry consistent with a PE-AFE transition. The PE-AFE transition for $x = 0.20$ is coincident with the relaxation behaviour present in all samples and hence cannot be resolved.

TEM and electron diffraction were used to further characterise changes in domain structure and crystal structure for samples of $x = 0.05$, 0.20 and 0.35. A dark field image of $x = 0.05$, with corresponding ⟨110⟩ zone axis diffraction patterns (ZADPs) inset is shown in Figure 7. The two patterns are from different macrodomains within the grain and reveal the variance of the ½{*ooo*} superstructure reflections which appear in 6/12 ⟨110⟩ ZADPs for *R3c* symmetry ($a^-a^-a^-$), according to Woodward and Reaney.[24] Figure 7 illustrates two domain length scales: fine scale ferroelectric/ferroelastic twin domains (10-20 nm) and larger regions (100-200 nm) which define the domain structure associated with antiphase tilting. This suggests the local directions of polarisation and strain (10-20 nm) are inconsistent with the rhombohedral distortion of the macroscopic tilt system and symmetry. To rationalise, the observed macroscopic symmetry (*R3c*), macrodomain and nanodomain structure, we propose that each tilt domain (100-200 nm) is an amalgamation of many tens of finer scale ferroelastic/ferroelectric twins (10-20 nm) whose average polarisation vector and spontaneous strain are consistent with the symmetry of the macroscopic tilt system ($a^-a^-a^-$) but which locally have lower symmetry. The most likely symmetry based on the diffraction patterns and domain structure is monoclinic. This scenario is schematically illustrated in Figure 8.

A bright field image of sample $x = 0.20$ along with <001>, <110>, and <111> ZADPs are shown in Figure 9. In agreement with Karimi *et al*,[9] an intermediate phase is observed which is quadrupled according to the $PbZrO_3$ structure with *Pbam* symmetry. The quadrupling arises from antipolar order of the A-site cations along <110> directions. Note however, that the ¼{*ooe*} reflections are streaked, indicating some variation in the cell

dimensions in 1D, an effect discussed in detail for doped $PbZrO_3$ structured ceramics by Maclaren et al.[25] In addition, ½{*ooo*} superstructure reflections are observed, consistent with the $a^0b^-b^-$ tilt system associated with the $PbZrO_3$-like structure.[26] Samples with x = 0.20 exhibit a typical lamellar ferroelastic domain structure (100-200 nm) consistent with previous studies of $PbZrO_3$ structured ceramics [27] but there is no evidence of the fine scale twins observed in x = 0.05.

A bright field image of x = 0.35 is shown in Figure 10 along with <001>, <110>, and <111> ZADPs. Very few grains revealed a clear domain structure, suggesting each is effectively a single domain. Electron diffraction patterns reveal a dominant superstructure that gives rise to a combination of ½{*ooo*}, ½{*eoo*} and ½{*eeo*} reflections, defining the likely tilt system as $a^-a^-c^+$ consistent with *Pnma* symmetry.[24] Although the dominant discrete superstructure reflections may be indexed according to a *Pnma* cell, there are diffuse reflection which lie at ~1/4{*ooe*} positions similar to those observed for x = 0.20. The appearance of 1/4{*ooe*} reflections and their diffuse character suggests there is still some tendency towards quadrupling of the cell in a manner reminiscent of $PbZrO_3$. The diffuse reflections imply residual short range, antipolar clustering of the A-site ions such that there is simultaneously a strong commensurate doubling of the cell in accordance with *Pnma* symmetry ($a^-a^-c^+$) but also a short range incommensurate modulation with a wavelength of ~$2\sqrt{2}a$.

The electrical microstructure and bulk conductivity of the ceramics were investigated using IS. A representative Z^* plot for x = 0.05 at ~ 350 ^oC is shown in Figure 11 (a) which gives rise to a single semi-circular arc that could be modelled, to a first approximation, on an equivalent circuit based on a single parallel Resistor-Capacitor (RC) element. The associated capacitance of the arc was ~ 16 $pFcm^{-1}$ indicating a bulk (grain) response that dominated the resistivity of the ceramic. The peak maximum in M'' is inversely proportional to C, and the peak maximum in Z'' is directly proportional to R.[28] The coincidence in frequency of the peak maximum in Z'' and M'' spectra in Figure 11 (b) demonstrated the ceramic to be electrically homogenous and this feature was observed in all samples. The activation energy for bulk conduction was calculated from Arrhenius plots of the bulk conductivity, σ (=1/R) and was > 1 eV for all compositions, Figure 12. This showed all samples to be electrically insulating and although the conduction mechanism is unknown at this stage the leaky behaviour displayed by undoped BFO has clearly been suppressed in this series of ceramics. A room temperature polarization *vs* electric field loop for x = 0.05 is shown in Figure 13 and is representative of all samples. The relationship between polarization and electric field is almost linear for all compositions and no switching was observed despite the large applied fields.

General Discussion

The discrete structural changes observed by XRD and dielectric data as a function of composition and temperature married to the absence of a second arc in the impedance spectroscopy measurements indicate that the ceramics are structurally and electrically homogeneous. Presumably, the enhanced homogeneity in comparison with previous studies of La doped $BiFeO_3$[9] arises because of the formation of A-site vacancies ($Ti_{Fe}^{\cdot} = 1/3V_{La}'''$) which enhance diffusion rates. Nonetheless, for the first time in La doped $BiFeO_3$ compositions, the local and domain structure can be reliably interpreted without the influence of macroscopic chemical inhomogeneity. Most importantly, the frustration effects discussed and documented extensively in, e.g. the PZT phase diagram,[29] in the vicinity of phase

boundaries may be evaluated. In PZT, Woodward and Reaney[29] reported an unusual nanodomain structure at the AFE/FE phase boundary within the *R3m* phase. The observed nanodomains existed within larger domains and were interpreted as local monoclinic (*Pm*) regions which amalgamated to give an average *R3m* structure. For compositions at the AFE/FE boundary in this contribution a similar situation is observed but with greater clarity as the domain variants of the antiphase tilt structure are an order of magnitude greater than the ferroelastic/ferroelectric nanotwins. Levin and Reaney[30] observed a similar phenomenon in $Na_{1/2}Bi_{1/2}TiO_3$ ceramics which they reported to contain long range antiphase tilt regions (μm) inside which ferroelastic/ferroelectric nanotwins (10-20 nm) resided.

The observation of short range antipolar order in the PE phase for compositions with x = 0.35 has no parallels with PZT since there is no room temperature PE phase reported in the associated phase diagram. Nonetheless, the concept of polar clusters (short range order) existing above the PE-FE T_C in ferroelectrics is very well accepted. Polar clusters are however, effectively invisible to diffraction techniques since there is no additional superstructure generated. If a similar phenomenon were considered above the PE-AFE T_C then weak, diffuse ¼{*ooe*} would be the natural consequence and are observed in the present study.

The BLFT solid solution series may therefore be considered to exhibit clear aspects of pseudosymmetry particularly in the vicinity of structural phase transitions. A pseudosymmetric composition is defined as containing a ubiquitous distribution of regions whose local symmetry is lower than the average macroscopic symmetry. The driving forces for the appearance of pseudosymmetry are nanoscale chemical distributions whose impact becomes most apparent as phase boundaries are approached and competition between local regions for the dominant symmetry is enhanced. Levin and co-workers[31] determined aspects of pseudosymmetry across the morphotropic phase boundary in $(Na,K)_{1/2}Bi_{1/2}TiO_3$ solid solutions in which similar generic features were described. Similarly, features of the morphotropic and AFE/FE phase boundaries in the PZT phase diagram[29] may be reinterpreted and attributed to the generic phenomenon of pseudosymmetry.

Conclusions

In summary, we present a study and interpretation of the phase transitions and domain structure in a new solid solution series, $(0.95-x)BiFeO_3$ - $xLaFeO_3$ - $0.05La_{2/3}TiO_3$. Samples were electrically homogeneous, with low dielectric loss (< 0.05) and bulk conduction activation energies in excess of 1 eV. TEM and XRD revealed a series of structural phase transitions, from *R3c* for samples with $x < 0.15$ to ($0.15 < x < 0.30$) and macroscopic *Pnma* phase for $x = 0.35$ with clusters of antipolar order. The dielectric data showed strong relaxation near T_N, however this did not impinge upon the broad anomalies which correspond to PE-AFE and PE-FE transitions. These anomalies occurred as a function of composition and were confirmed using *in-situ* XRD.

The domain structure in the FE phase near the AFE boundary was complex with ferroelastic nanotwin domains present, inconsistent with the macroscopic tilt domain structure. A model has been proposed where the macroscopic tilt domains are considered to be an amalgamation of lower symmetry twins in which the average macroscopic polarisation vector remains [111], consistent with the average symmetry by XRD. The presence of diffuse

1/4{*ooe*} reflections in addition to strong discrete, doubled superstructure reflections for x = 0.35 was considered as evidence that antipolar clusters were residual in the *Pnma* phase adjacent to the AFE/PE boundary.

Finally, it is concluded that aspects of pseudosymmetry may be clearly resolved in BLFT compositions through detailed TEM and electron diffraction studies in the vicinity of the phase boundaries where the local symmetry invariably appears lower than the average macroscopic symmetry.

Acknowledgements

AK acknowledges Abdul Wali Khan University Mardan for funding. All authors acknowledge the grant, Sustainability and Substitution of Functional Materials and Devices EPSRC (EP/L017563/1).

References

1. D. C. Arnold, K. S. Knight, F. D. Morrison and P. Lightfoot, Physical Review Letters **102**, 027602 (2009).
2. P. Fischerl, M. PoIomska, I. Sosnowska and M. Szymanski, J. Phys. C: Solid State Phys. **13**, 1931 (1980).
3. I. Sosnowska, T. Peterlin-Neumaier and E. Steichele, J. Phys. C: Solid State Phys. **15**, 4835-4846 (1982).
4. F. Kubel and H. Schmid, Acta cryst. **B46**, 698(1990).
5. J. M. Moreau, C. Michel, R. Gerson and W. J. James, J. Phys. C: Solid State Phys. **32**, 1315 (1970).
6. J. Neaton, C. Ederer, U. Waghmare, N. Spaldin and K. Rabe, Physical Review B **71**, (2005).
7. V. V. Shvartsman, W. Kleemann, R. Haumont and J. Kreisel, Applied Physics Letters **90**, 172115 (2007).
8. G. Catalan and J. F. Scott, Advanced Materials **21**, 2463 (2009).
9. S. Karimi, I. Reaney, Y. Han, J. Pokorny and I. Sterianou, Journal of Materials Science **44**, 5102 (2009).

10. M. Fiebig, Journal of Physics D: Applied Physics **38**, R123 (2005).
11. K. Kalantari, I. Sterianou, D. C. Sinclair, P. A. Bingham, J. Pokorný and I. M. Reaney, Journal of Applied Physics **111**, 064107 (2012).
12. M. S. Bernardo, T. Jardiel, M. Peiteado, A. C. Caballero and M. Villegas, Journal of the European Ceramic Society **31**, 3047 (2011).
13. S. Karimi, I. M. Reaney, I. Levin and I. Sterianou, Applied Physics Letters **94**, 112903 (2009).
14. X. Qi, J. Dho, R. Tomov, M. G. Blamire and J. L. MacManus-Driscoll, Applied Physics Letters **86**, 062903 (2005).
15. K. Kalantari, I. Sterianou, S. Karimi, M. C. Ferrarelli, S. Miao, D. C. Sinclair and I. M. Reaney, Advanced Functional Materials **21**, 3737 (2011).
16. I. M. Reaney, I. MacLaren, L. Wang, B. Schaffer, A. Craven, K. Kalantari, I. Sterianou, S. Miao, S. Karimi and D. C. Sinclair, Applied Physics Letters **100**, 182902 (2012).
17. P. Goudochnikov and A. J. Bell, Journal of physics. Condensed matter : an Institute of Physics journal **19**, 176201 (2007).
18. V. M. Goldschmidt, Naturwissenschaften **14**, 477 (1926).
19. R. D. Shannon, Journal of Applied Physics **73**, 348 (1993).
20. Y.-K. Jun, W.-T. Moon, C.-M. Chang, H.-S. Kim, H. S. Ryu, J. W. Kim, K. H. Kim and S.-H. Hong, Solid State Communications **135**, 133 (2005).
21. C. J. Cheng, D. Kan, S. H. Lim, W. R. McKenzie, P. R. Munroe, L. G. Salamanca-Riba, R. L. Withers, I. Takeuchi and V. Nagarajan, Physical Review B **80**, 014109 (2009).
22. V. Goian, S. Kamba, S. Greicius, D. Nuzhnyy, S. Karimi and I. M. Reaney, Journal of Applied Physics **110**, 074112 (2011).

23. Y. F. Cui, Y. G. Zhao, L. B. Luo, J. J. Yang, H. Chang, M. H. Zhu, D. Xie and T. L. Ren, Applied Physics Letters **97**, 222904 (2010).

24. D. I. Woodward and I. M. Reaney, Acta crystallographica. Section B, Structural science **61**, 387 (2005).

25. I. MacLaren, R. Villaurrutia and A. Peláiz-Barranco, Journal of Applied Physics **108**, 034109 (2010).

26. A. M. Glazer, Acta cryst. Sect B **B49**, 846-852 (1993).

27. S. R. Tanaka M, Tsuzuki K, Jpn. J. Appl. Phys. **21**, 291 (1982).

28. D. C. Sinclair and A. R. West, Journal of Applied Physics **66**, 3850 (1989).

29. D. I. Woodward, J. Knudsen and I. M Reaney, Phys. Rev. B 72 (10) 104110 (2005).

30. I. Levin, I. M Reaney, Adv. Funct. Mater., 22(16) 3445 (2012).

31. I Levin, IM Reaney, EM Anton, Wook Jo, J Rödel, J Pokorny, LA Schmitt, HJ Kleebe, M Hinterstein, JL Jones, Phys. Rev. B, 87(2) 024113 (2013).

List of Figures

Figure 9: Bright field TEM showing ferroelastic domains typical of the PZ-like structure. Inset are <100>, <011> and <111> ZADPs. *af* = ¼{hk0} reflections associated with antipolar order in the PZ-like structure. *a* = ½{ooo} reflections associated with antiphase rotations of the octahedra and consistent with an $a^0b^-b^-$ tilt system.

Figure 10: Bright field image and <<001>, <110, and <111> zone axis diffraction patterns from compositions with *x* = 0.35. ½{*eeo*} superstructure reflections are denoted '*ac*' and arise from antiparallel cation displacement, ½{ooe} reflections (*i*) arise from in phase tilting, ½{ooo} (*a*) are generated by antiphase tilting. Diffuse ¼{ooe} (*af*) reflections arise from antipolar clusters and are highlighted in the expanded inset.

Figure 11: (a) Z* and (b) a combined *Z″* and *M″* spectroscopic plot for *x* = 0.05 at 347 ^{o}C.

Figure 12: Arrhenius plots of bulk conductivity for BLFT ceramics.

Figure 13: Polarization *vs* electric field for *x* = 0.05 at room temperature.

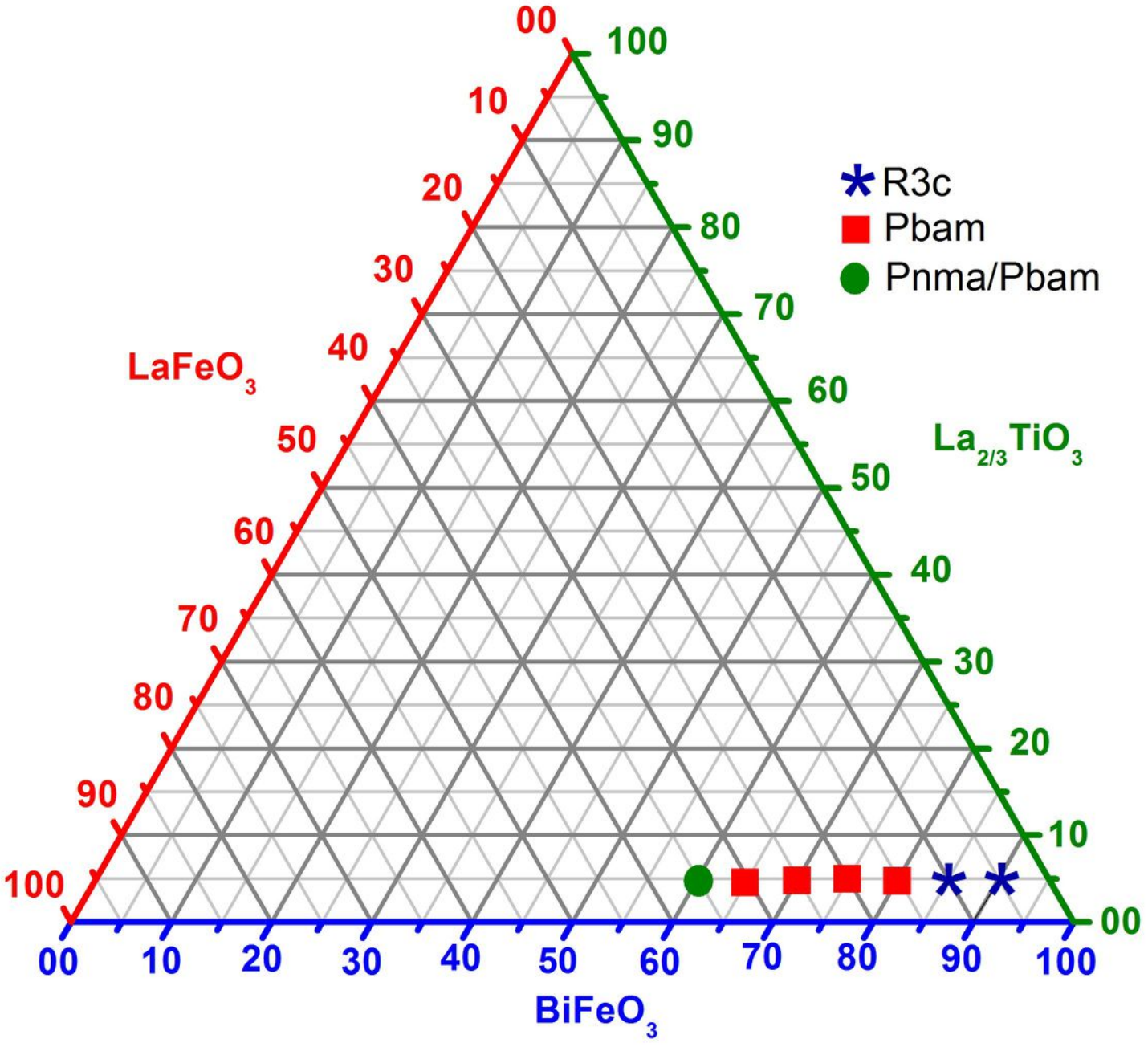
00
10
20
30
40
50
60
70
80
90
100
LaFeO3
100
90
80
70
60
50
40
30
20
10
00
La2/3TiO3
00
10
20
30
40
50
60
70
80
90
100
BiFeO3
R3c
Pbam
Pnma/Pbam

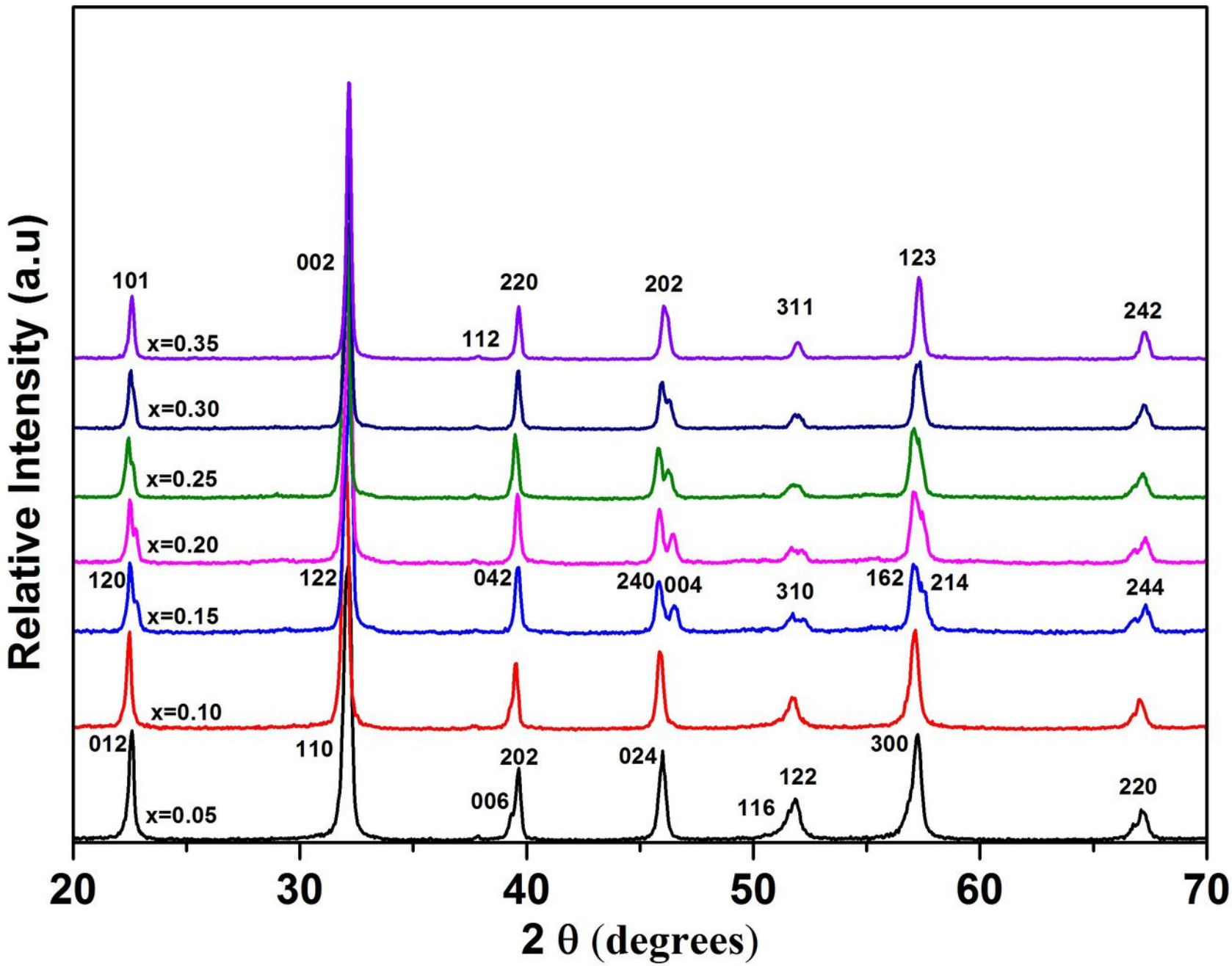
Relative Intensity (a.u)
2 θ (degrees)
20
30
40
50
60
70
x=0.35
x=0.30
x=0.25
x=0.20
x=0.15
x=0.10
x=0.05
101
002
112
220
202
311
123
242
120
122
042
240
004
310
162
214
244
012
110
006
202
024
116
122
300
220

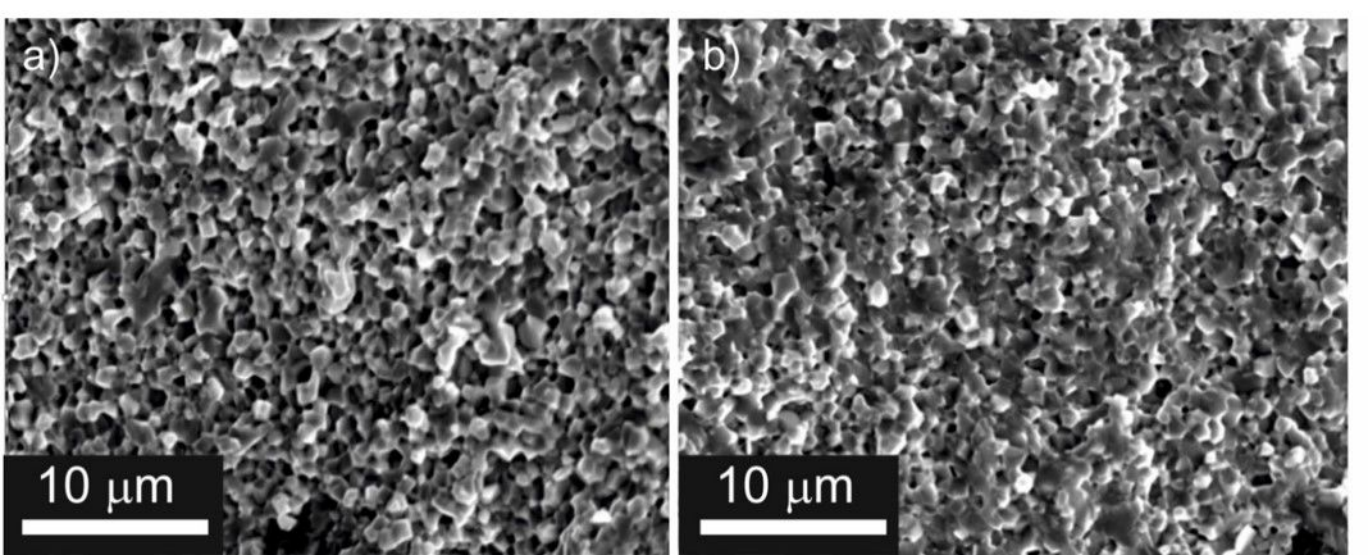
a)
10 μm
b)
10 μm

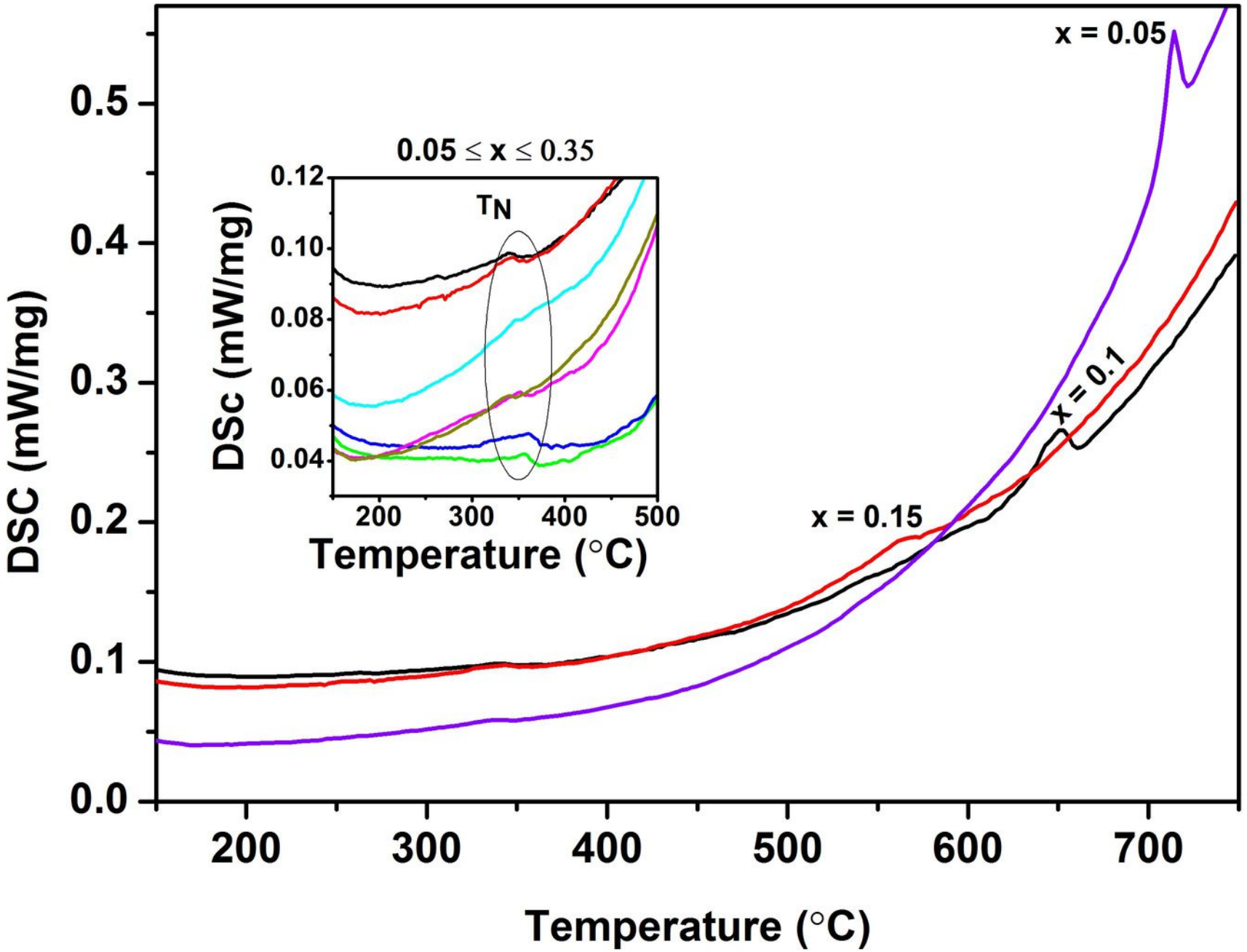
DSC (mW/mg)
0.0
0.1
0.2
0.3
0.4
0.5
200
300
400
500
600
700
Temperature (°C)
x = 0.05
x = 0.1
x = 0.15
0.05 ≤ x ≤ 0.35
DSc (mW/mg)
0.04
0.06
0.08
0.10
0.12
TN
200
300
400
500
Temperature (°C)

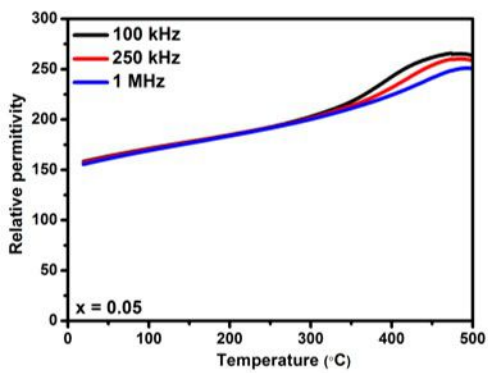
100 kHz
250 kHz
1 MHz
Relative permitivity
x = 0.05
Temperature (°C)

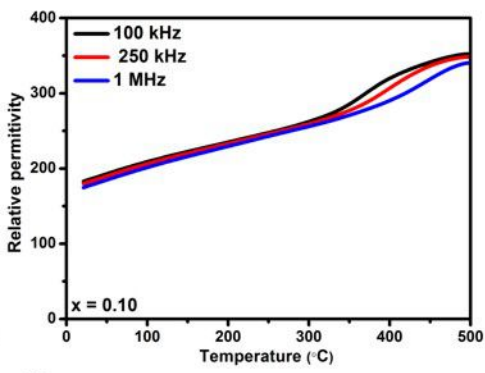
100 kHz
250 kHz
1 MHz
Relative permitivity
x = 0.10
Temperature (°C)

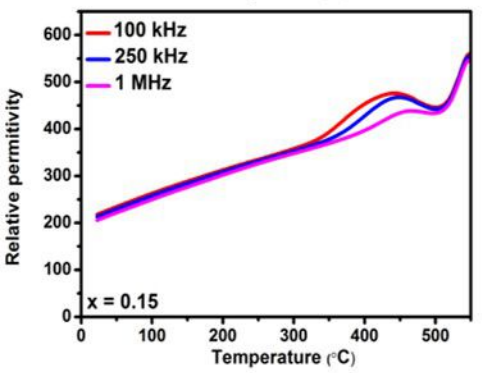
100 kHz
250 kHz
1 MHz
Relative permitivity
x = 0.15
Temperature (°C)

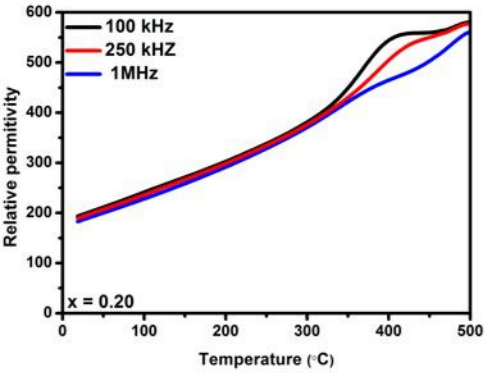
100 kHz
250 kHZ
1MHz
Relative permitivity
x = 0.20
Temperature (°C)

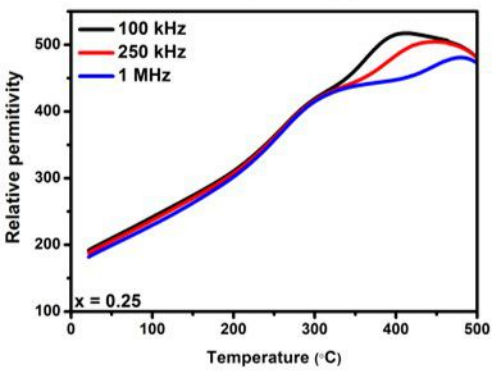
100 kHz
250 kHz
1 MHz
Relative permitivity
x = 0.25
Temperature (°C)

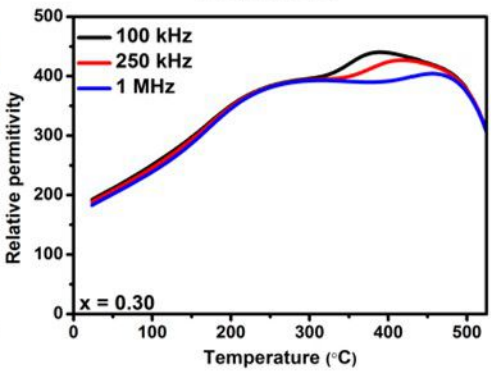
100 kHz
250 kHz
1 MHz
Relative permitivity
x = 0.30
Temperature (°C)

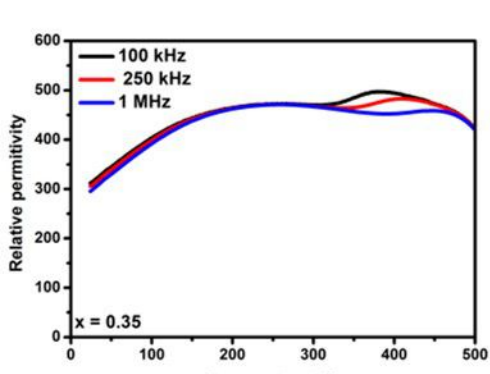
100 kHz
250 kHz
1 MHz
Relative permitivity
x = 0.35
Temperature (°C)

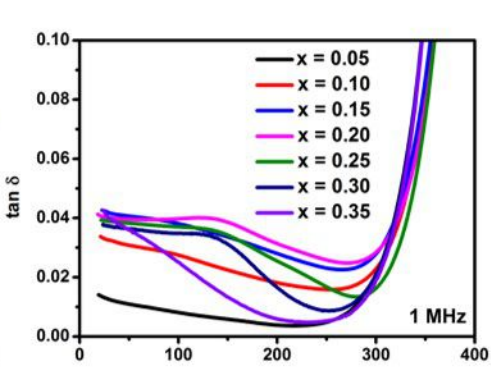
x = 0.05
x = 0.10
x = 0.15
x = 0.20
x = 0.25
x = 0.30
x = 0.35
tan δ
1 MHz
Temperature (°C)

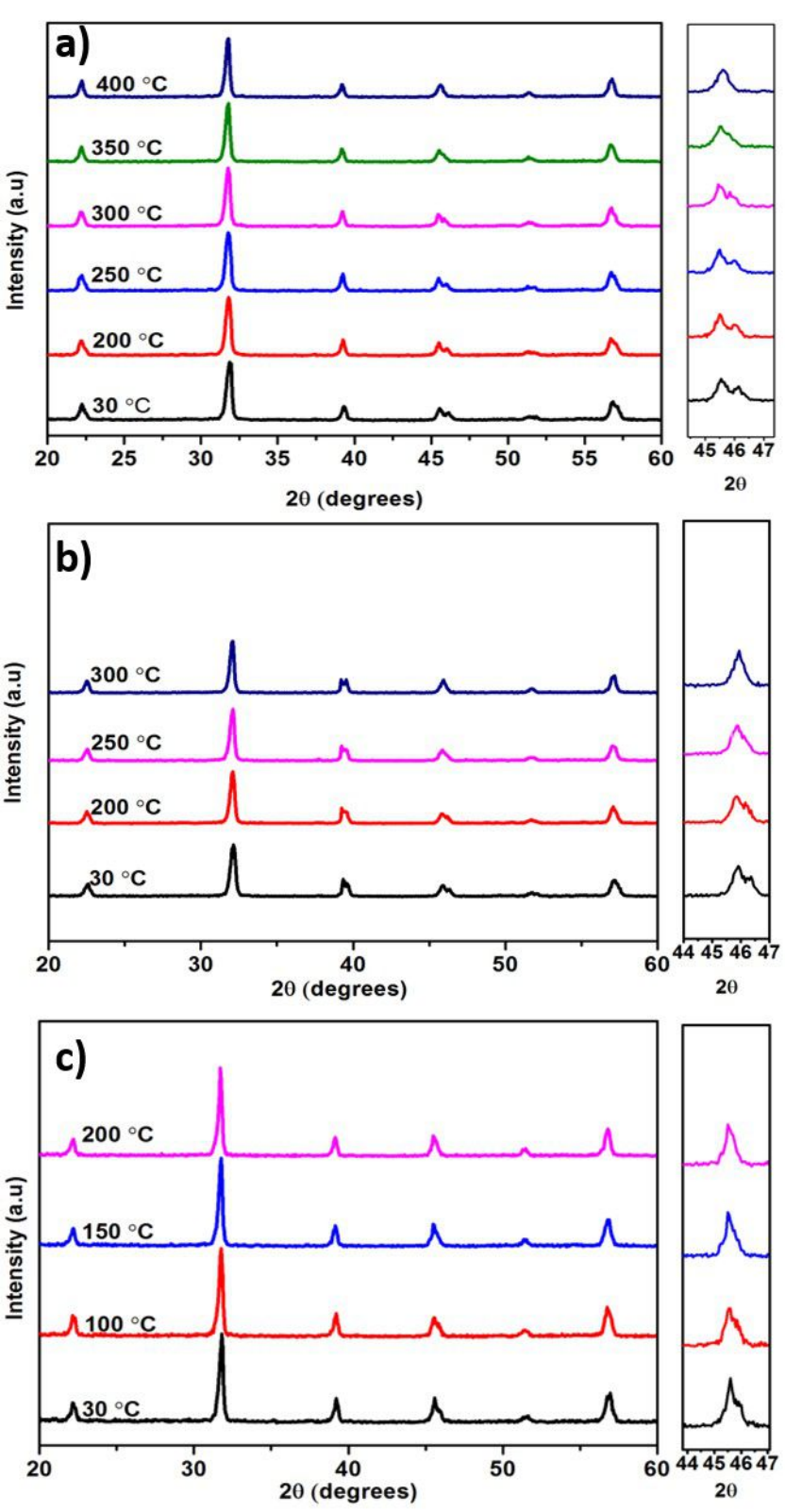
a)
400 °C
350 °C
300 °C
250 °C
200 °C
30 °C
Intensity (a.u)
20 25 30 35 40 45 50 55 60
2θ (degrees)
45 46 47
2θ
b)
300 °C
250 °C
200 °C
30 °C
Intensity (a.u)
20 30 40 50 60
2θ (degrees)
44 45 46 47
2θ
c)
200 °C
150 °C
100 °C
30 °C
Intensity (a.u)
20 30 40 50 60
2θ (degrees)
44 45 46 47
2θ

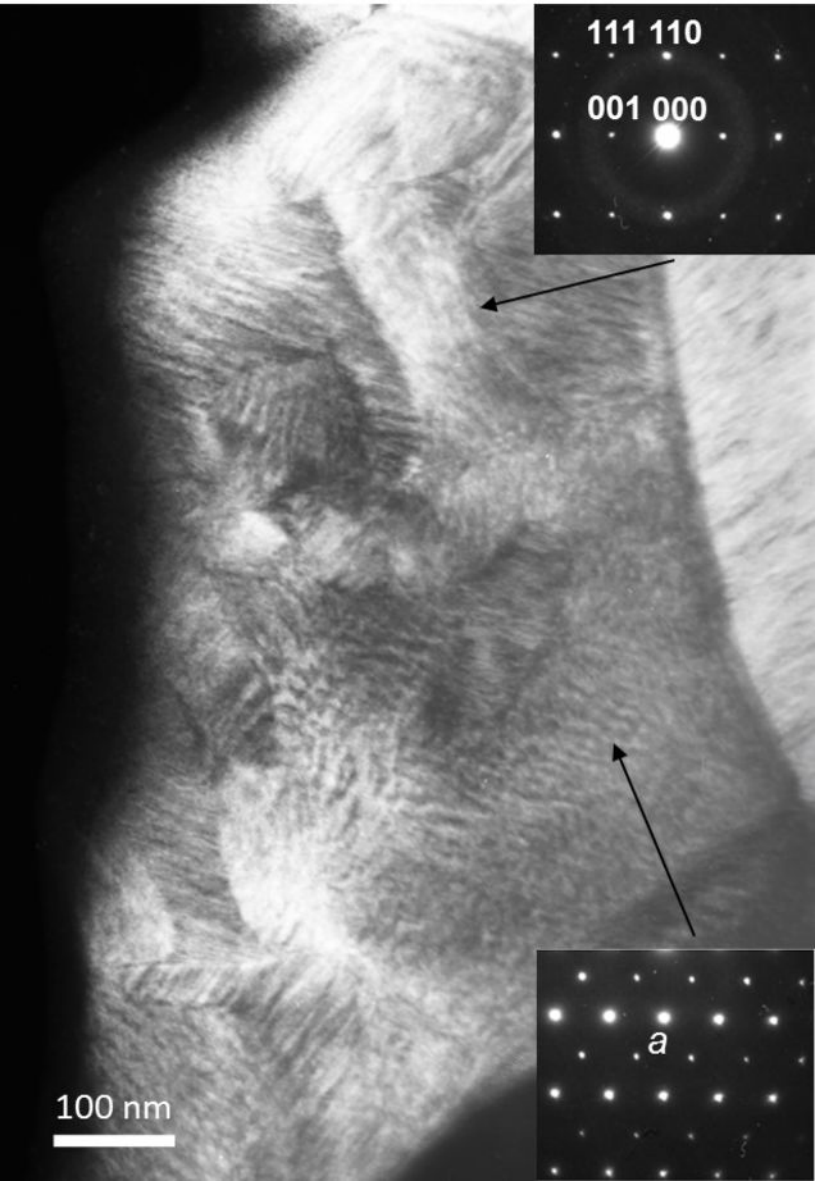
111 110
001 000
a
100 nm

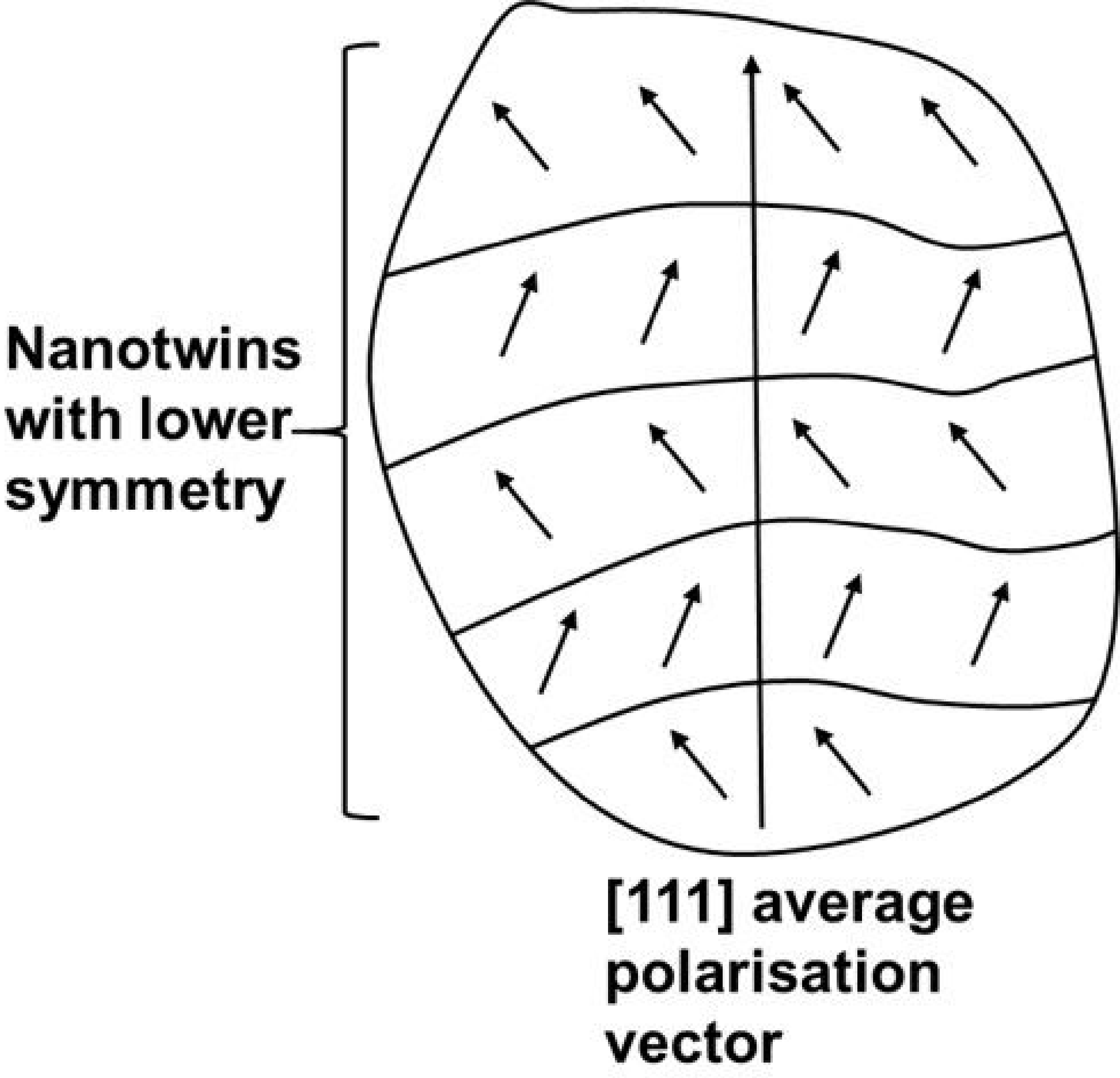
Nanotwins with lower symmetry
[111] average polarisation vector

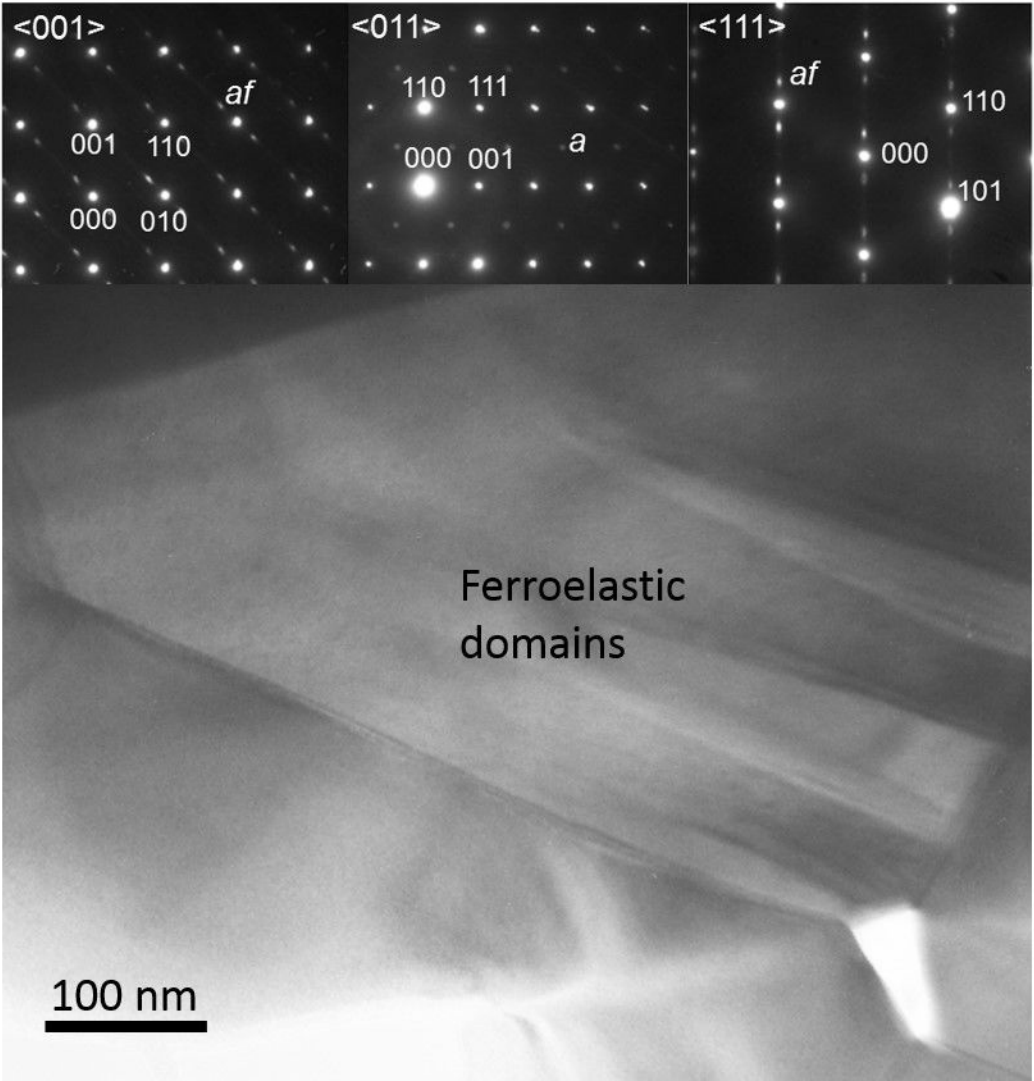
<001>
af
001
110
000
010
<011>
110
111
a
000
001
<111>
af
110
000
101
Ferroelastic
domains
100 nm

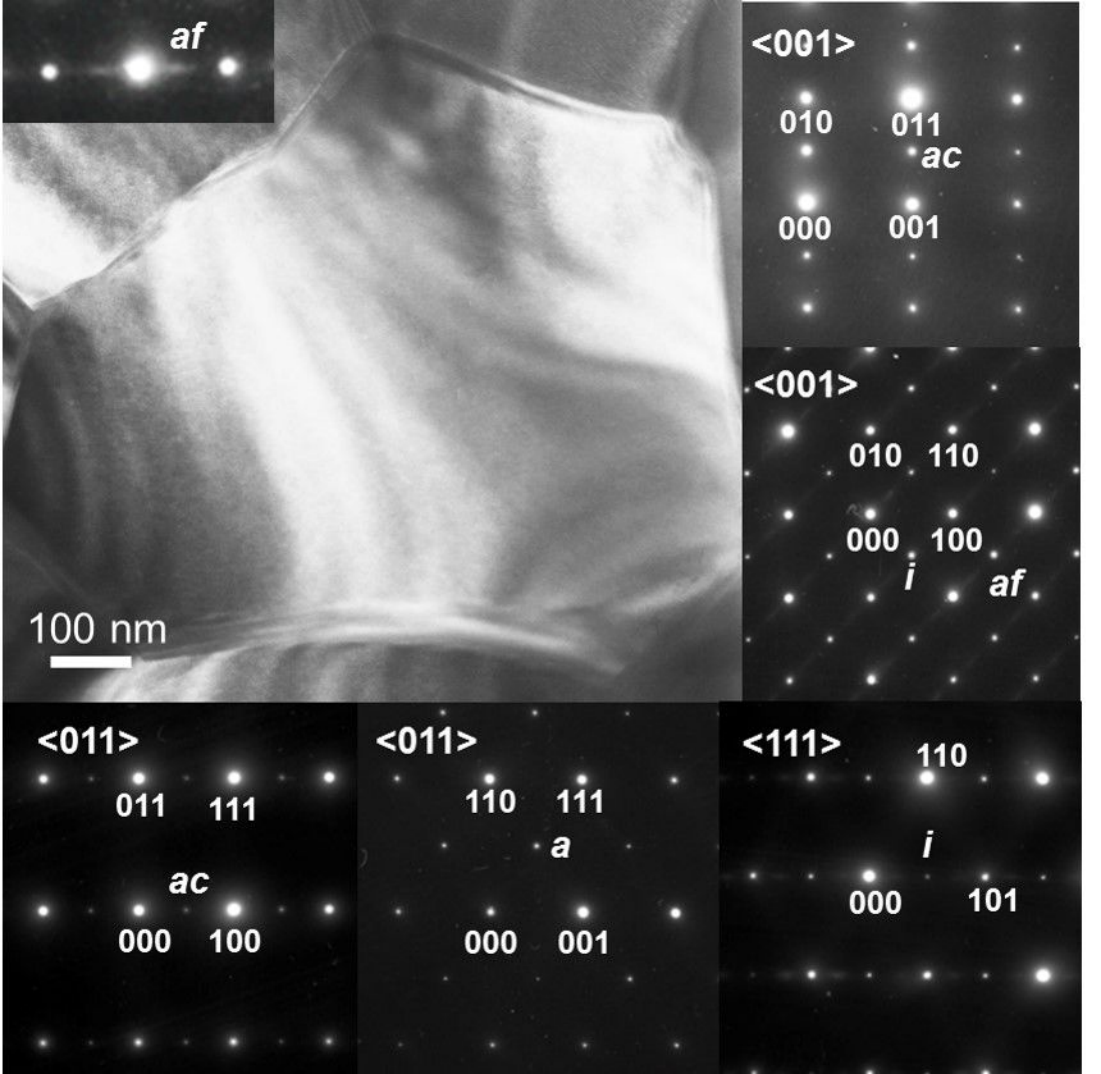
af
<001>
010
011
ac
000
001
<001>
010
110
000
100
i
af
100 nm
<011>
011
111
ac
000
100
<011>
110
111
a
000
001
<111>
110
i
000
101

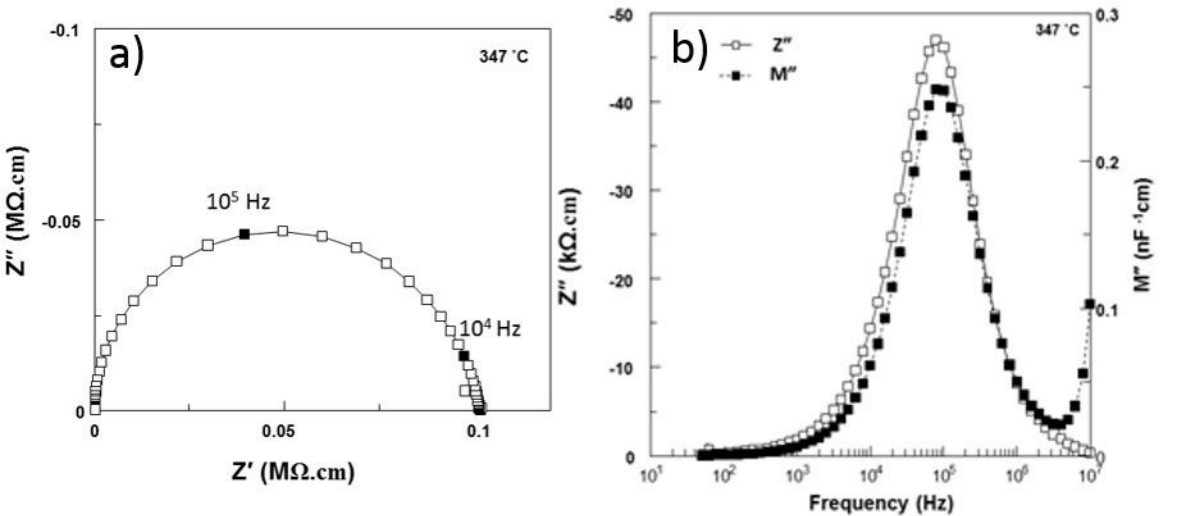
a)
347 °C
10^5 Hz
10^4 Hz
-0.1
-0.05
0
0
0.05
0.1
Z′ (MΩ.cm)
Z″ (MΩ.cm)
b)
Z″
M″
347 °C
-50
-40
-30
-20
-10
0
0.3
0.2
0.1
10^1
10^2
10^3
10^4
10^5
10^6
10^7
Frequency (Hz)
Z″ (kΩ.cm)
M″ (nF⁻¹cm)

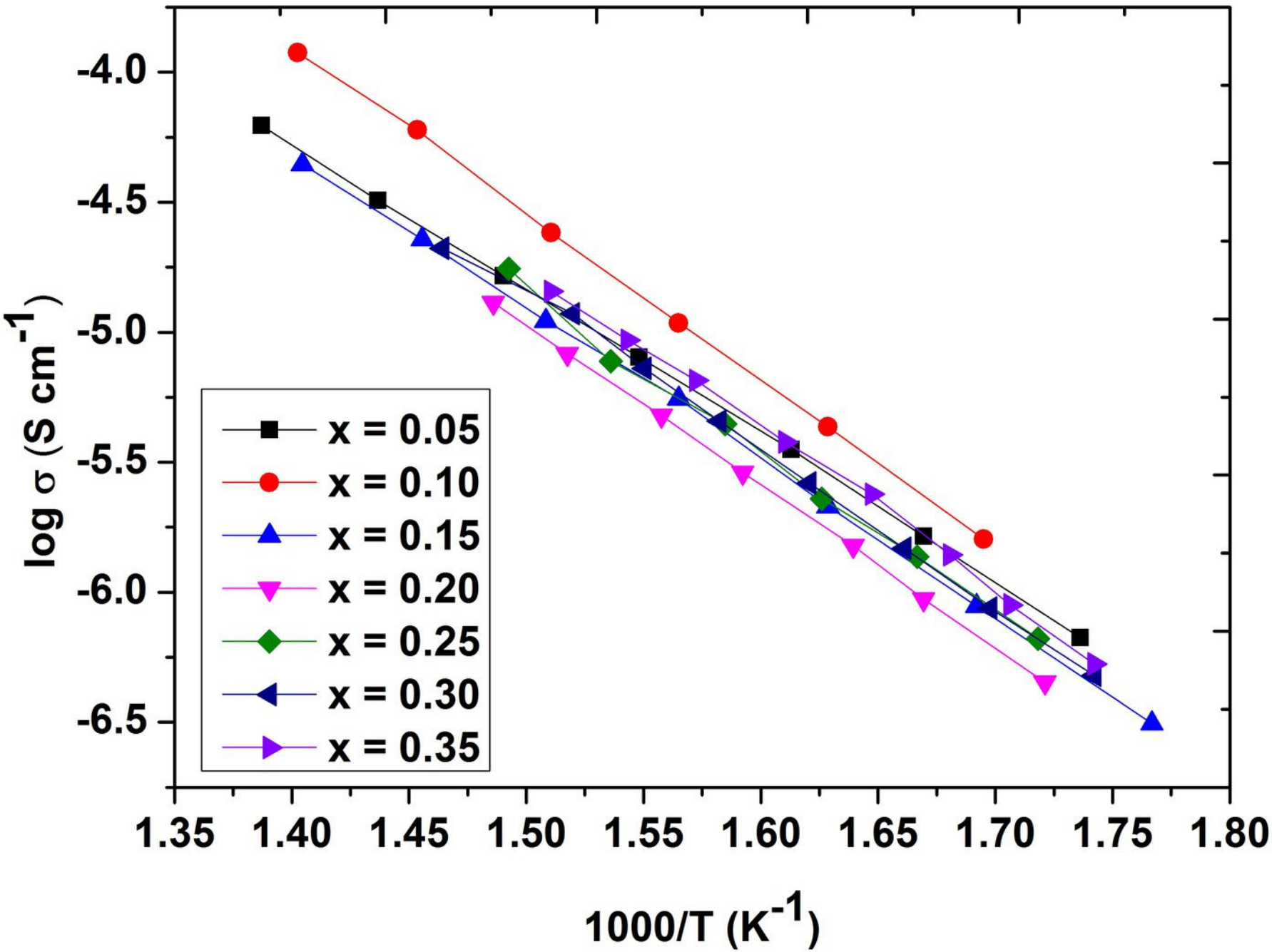
-4.0
-4.5
-5.0
-5.5
-6.0
-6.5
log σ (S cm-1)
1.35
1.40
1.45
1.50
1.55
1.60
1.65
1.70
1.75
1.80
1000/T (K-1)
x = 0.05
x = 0.10
x = 0.15
x = 0.20
x = 0.25
x = 0.30
x = 0.35

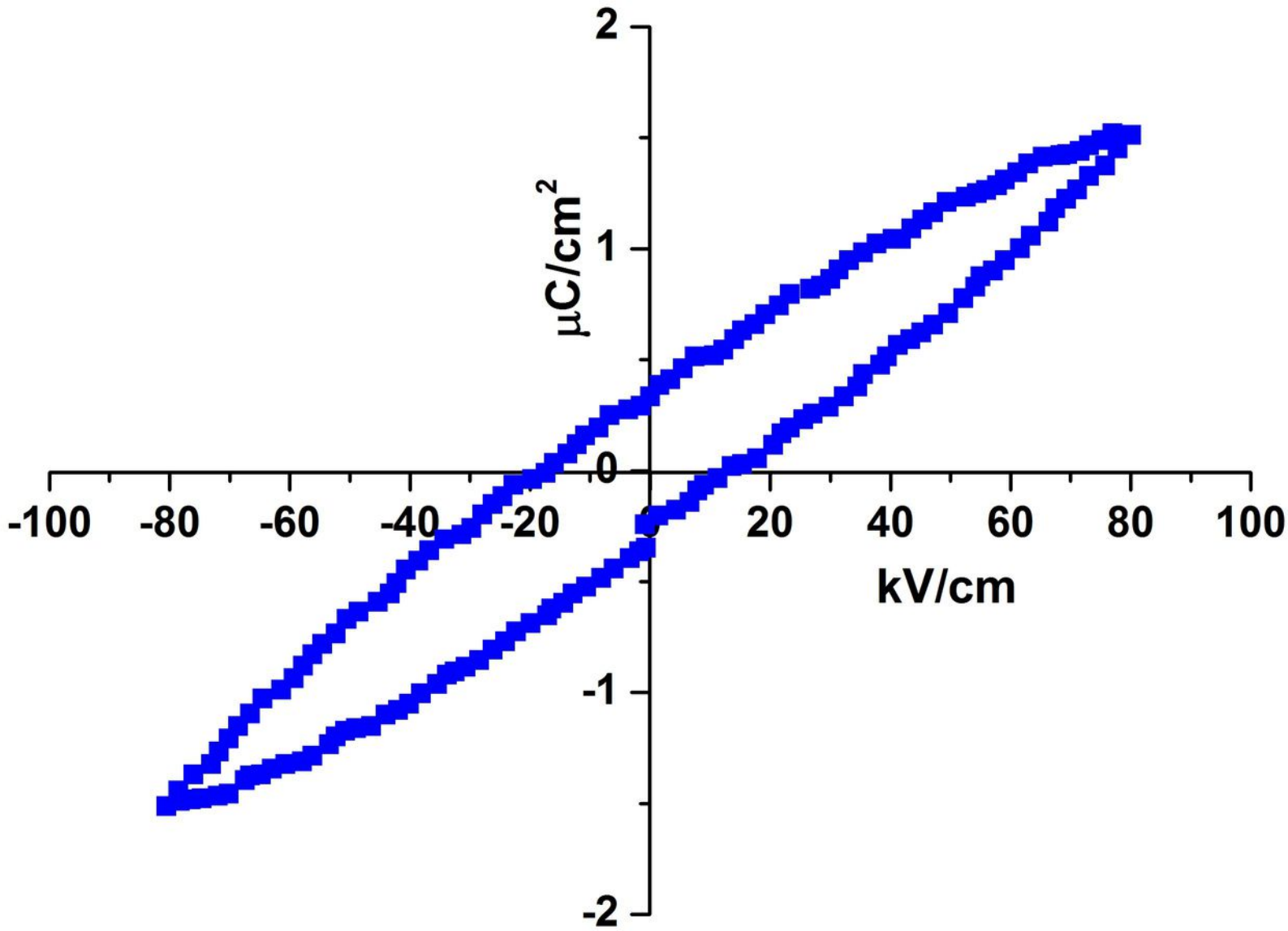
2
1
0
-1
-2
μC/cm²
-100
-80
-60
-40
-20
20
40
60
80
100
kV/cm